ARTICLE

Electrochemical polarization behavior and superelastic properties of a Fe–Mn–Al–Ni–Cr shape memory alloy

Johanna-Maria Frenck 🔾 | **Malte Vollmer** | **Thomas Niendorf**

Department of Mechanical Engineering, Institute of Materials Engineering, University of Kassel, Kassel, Germany

Correspondence

Johanna-Maria Frenck, Department of Mechanical Engineering, Institute of Materials Engineering, University of Kassel, Moenchebergstraße 3, 34125 Kassel, Germany.
Email: j.frenck@uni-kassel.de

Abstract

The present study investigates the corrosion behavior of a Fe–Mn–Al–Ni–Cr shape memory alloy in a 5.0 wt% NaCl solution in combination with the functional properties. In a single crystalline condition, the investigated alloy shows a superior superelastic response with a maximum recovery strain of 5.2%. Furthermore, the results of the potentiodynamic polarization and impedance spectroscopy show that the addition of chromium generally improves corrosion resistance by increasing the resistance to localized corrosion. The single crystalline condition, which is characterized by an austenitic matrix and scattered martensite plates, shows an enhanced, however, still unstable passive behavior due to the formation of corrosion pits along the martensite plates.

KEYWORDS

electrochemical impedance spectroscopy, Fe–Mn–Al–Ni–Cr, iron-based shape memory alloy, passive films, pitting corrosion, potentiodynamic polarization, pseudoelasticity

1 | INTRODUCTION

Shape memory alloys (SMAs) are materials characterized by a thermoelastic, martensitic phase transformation. Due to the fully reversible transformation between a high-temperature phase (austenite) and a low-temperature phase (martensite), these alloys are able to recover their original shape after deformation. Among other applications, SMAs are promising for structural engineering applications, such as damping elements for high-rise buildings in earthquake-prone areas[1] or as reinforcement or prestressing elements in concrete structures.[2,3] Iron-based SMAs are most promising for those large-scale and mass-intensive applications, due to relatively low material and manufacturing costs. In contrast to other iron-based SMAs such as Fe–Mn–Si–X (X = Cr, Al, Cu, Ni) or Fe–Ni–Co–Al–Y (Y = Ti, Nb, Ta)

the Fe–Mn–Al–Ni alloy (FMAN), which was first introduced in 2011,[4] shows an unusual martensitic transformation between an α (bcc) austenite and γ′ (fcc) martensite phase, very good superelastic properties at room temperature and a low-temperature dependence of the martensitic transformation.[4] However, the superelastic properties of FMAN are strongly influenced by various factors such as grain size,[5–10] crystallographic orientation,[11–14] and precipitates.[15–17] While a single crystalline or oligocrystalline condition can show a superelastic recoverability up to 10%,[5,10,12,13,15,16,18] the superelastic behavior of polycrystalline conditions is mainly restricted due to pronounced constraints resulting from neighboring grains during transformation.[5,6] In addition to the influence of grain size, it was shown that a small amount of ductile γ-phase along the grain boundaries is required to suppress intergranular

cracking in oligocrystalline, although γ-phase is generally detrimental in terms of the functional response since it does not participate in the phase transformation.[19] For an application in structural engineering, besides the mechanical properties, the behavior of the material under corrosive conditions is a decisive factor. Up to now, only a few corrosion studies have been performed aiming to investigate the effects of different microstructures and different electrolytic solutions on the corrosion behavior of the FMAN alloy system. Data published so far indicate that FMAN behaves similarly to pure iron in a 5.0 wt% NaCl solution (pH 6–7)[20] as well as in a saturated $Ca(OH)_2$ solution (pH 12–13).[21] However, in contrast to pure iron, a single crystalline condition shows the formation of an unstable passive layer during polarization measurements in the NaCl solution.[20] Thus, to improve the corrosion properties of FMAN, a key objective for future investigations should be the stabilization of the passivating behavior. However, at the same time, good functional properties have to be preserved. In contrast to FMAN, numerous studies focusing on the corrosion properties of the Fe–Mn–Si–X SMA system have been conducted. By adding chromium a significant improvement in the corrosion behavior was achieved.[22–28] As similar effects were also observed for high Mn steels (these being only used for structural applications) with a chromium content of 1–3 wt%,[29] it seems reasonable to assume that adding a chromium content of 1.5 at% (≙1.5 wt%) to the FMAN alloy could already enhance the corrosion properties. Xia et al.[30] already reported a good superelastic response for single crystalline specimens in the Fe–Mn–Al–Ni–Cr alloy system with chromium contents up to 7.5 at%. However, the corrosion behavior of these alloys has not yet been investigated. For this reason, the present study aims to fill this gap by investigating the influence of 1.5 at% chromium on the corrosion behavior of the FMAN alloy system. For this purpose, three specifically tailored

microstructures were investigated using electrochemical corrosion measurements, namely measurements of the open-circuit potential (OCP), potentiodynamic polarization (POL), and electrochemical impedance spectroscopy (EIS). The EIS measurements were conducted to evaluate the passivating oxide layer in more detail and to characterize the evolving structure using an equivalent circuit model. Following the polarization measurements, the corrosion damage in the cross-section of the specimens was analyzed by means of optical microscopy (OM) and scanning electron microscopy (SEM) including energy dispersive spectroscopy (EDS).

2 | EXPERIMENTAL

2.1 | Alloy design and heat treatment

An ingot, with the chemical composition (determined by X-ray fluorescence spectroscopy) of Fe–34.72%Mn–13.35% Al–7.67%Ni–1.54%Cr (at%; FMAN–Cr), was produced using vacuum induction melting. Compression specimens with a size of 3 mm × 3 mm × 6 mm and cylindrical corrosion specimens with a height and diameter of 10 mm were cut using electrodischarge machining. Heat treatments to adjust the microstructures were performed under an argon atmosphere using the heat treatment procedures shown in Figure 1. Three different microstructural conditions were investigated. For the first condition, hereafter referred to as "furnace-cooled condition," the specimens were solution heat-treated (1225°C, 60 min) and afterward slowly furnace-cooled (Figure 1a). To obtain a "polycrystalline condition" several specimens were solution heat-treated for 60 min and then water quenched (wq) in 80°C warm water (Figure 1a). The cyclic heat treatment (Figure 1b) was performed to achieve a "single crystalline condition." In addition, to enhance the superelastic properties, the compression specimens were aged at 200°C for 180 min before the
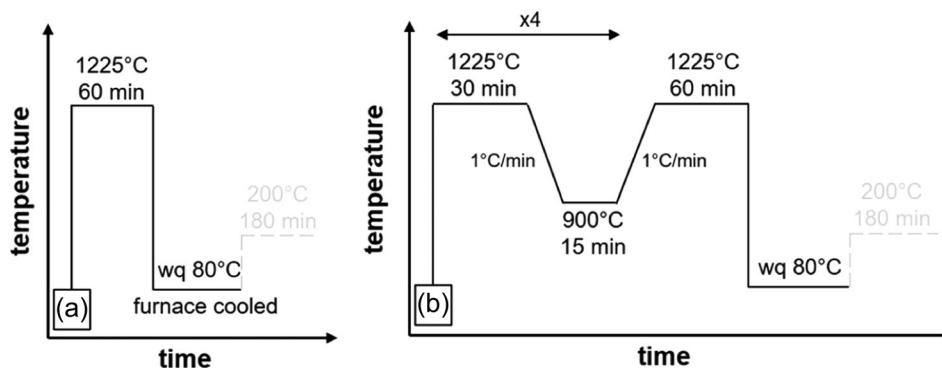

FIGURE 1 Heat treatment procedures applied to establish (a) the furnace-cooled and polycrystalline conditions, (b) the single crystalline condition of Fe–Mn–Al–Ni–Cr. Compression specimens were additionally aged at 200°C for 180 min.

mechanical tests to form coherent B2 (bcc/NiAl) precipitates within the austenitic matrix.[30] No additional aging heat treatment has been performed on the corrosion specimens.

2.2 | Microstructure analysis and incremental strain tests

After the heat treatment, compression specimens were ground down to 5-μm grit size and vibro-polished for 2 h using a colloidal SiO_2 suspension with 0.02 μm particle size. The subsequent electron backscatter diffraction (EBSD) measurements were performed using an SEM operated at 20 kV. EBSD maps with a size of approximately 3 mm × 6 mm were acquired at a step size of 40 μm. The α-phase (lattice parameter of 0.2903 nm) was used for indexing. The data obtained were analyzed using TSL OIM Analysis 7 software. The superelastic behavior was then evaluated at room temperature using incremental strain tests with a maximum strain of 6%. The experiments were carried out using a servo-hydraulic test rig equipped with a 63 kN load cell at a loading rate of 5 μm/s. Strains were measured using an extensometer with a 12-mm gauge length directly attached to the compression grips. The strains were then recalculated by assuming an infinite stiffness of the grips.

2.3 | Corrosion measurements

The lateral surfaces of the cylindrical corrosion specimens were ground down to 5-μm grit size. The base areas were concealed using an acid-resistant lacquer, eventually leaving only the lateral area as a well-defined corrosion area of approximately 3.14 cm². Specimens were again ground directly before the electrochemical measurements, subsequently cleaned with distilled water and ethanol, and immediately placed into the test solution. The electrochemical measurements were performed using a Gamry Potentiostat 3000 with a conventional three-electrode cell system, in an aerated 5.0 wt% NaCl solution. A graphite rod and a saturated calomel electrode (SCE), with a value of −241 mV with respect to the standard hydrogen electrode, were used as the counter electrode and the reference electrode, respectively. The corrosion specimens were used as the working electrode. All potentials in this study are reported with respect to the value of the SCE. The OCP was measured for 24 h to ensure the evolution of a stable system before the EIS and POL measurements.

The POL measurements were initiated at about 300 mV with respect to E_{OCP} and were carried out up to the potential at which the anodic polarization current density suddenly increased rapidly (passive film break down). The scan rate applied was 0.5 mV/s. Electrochemical parameters such as E_{corr} or i_{corr} were extracted from the polarization curves using the Gamry Echem Analyst software and the Tafel extrapolation method[31] in a range of ±100 mV with respect to E_{corr}. For application of the Tafel extrapolation, the curves have to exhibit a linear progression over a decade of the current density for both the anodic and cathodic regions.[32] In case the anodic reaction did not show a linear trend, analysis was performed only based on the cathodic curve. To investigate the passive layer that formed on the surface before the potentiodynamic scans EIS measurements were carried out immediately before the POL tests by applying an AC amplitude of 10 mV with respect to E_{OCP} in a frequency range from 10 kHz down to 10 mHz. Since data from EIS measurements are not yet available in the literature, EIS measurements were also performed on a single crystal of the well-established Fe–32.46%Mn–14.60%Al–7.37%Ni (at %; FMAN) alloy for comparison. The single crystalline condition was obtained using the cyclic heat treatment shown in Figure 2. Afterward, the specimen was prepared in the same way as the corrosion specimens of the FMAN–Cr alloy.
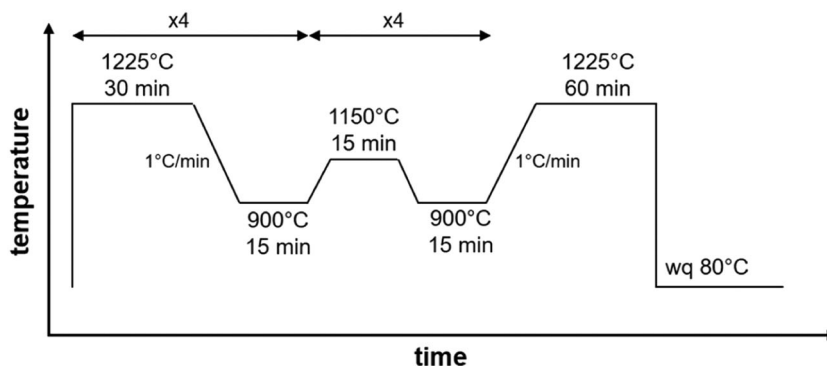

FIGURE 2 Heat treatment procedure applied to establish the single crystalline condition of Fe–Mn–Al–Ni for corrosion specimens. No additional aging heat treatment has been conducted.

2.4 | Postcorrosion microstructure analysis

Surface analysis was conducted to investigate the elementary contributions to the occurring corrosion attack in detail. To analyze the corrosion damage after the POL measurement in the cross-sectional area, the tested specimens were embedded in epoxy resin, ground to 5-µm grit size, and finally vibro-polished using a colloidal SiO_2 suspension with 0.02-µm particle size. Care was taken to ensure that the removed surface was at least 0.5-mm thick to exclude influences of the lacquer layer. The morphology of the corrosive attack and the formed oxide layers in the cross-section were analyzed by means of OM, SEM, and EDS. The SEM was operated at 20 kV. EDS measurements have been conducted and analyzed using the EDAX Genesis 6.28 Software.

3 | RESULTS AND DISCUSSION

Figure 3a displays the optical micrograph (OM) and Figure 3b–g SEM data including EDS element maps of the furnace-cooled condition of FMAN–Cr. Due to the slow cooling rate, the formation of three different phases can be observed. Thus, in contrast to the FMAN alloy with the same heat treatment procedure, where only two different phases form,[20] the formation of an additional phase is observed. According to the phase diagram of FMAN shown in the study by Frenck et al.,[20] two of the phases being present can be related to γ-phase (light gray areas) and β-Mn-phase (patterned dark gray areas). For both alloys (FMAN and FMAN-Cr), quantitative data for the phase fraction were obtained based on a gray scale analysis considering OM images. The OM images used for the phase fraction analysis can be found in Figure S1. Figure S1a has been recompiled from the study by Frenck et al.[20] The analysis was done using the ImageJ 2 software. Similar γ-phase fractions were determined for FMAN and FMAN–Cr. While the FMAN alloy consists of about 65% γ-phase the fraction increases for the FMAN–Cr alloy to approximately 75%. Furthermore, the evaluation of the EDS element maps indicates that both, the γ-phase as well as the β-Mn-phase, generally have a chemical distribution similar to the FMAN alloy.[20] The γ-phase is enriched with iron and manganese, while the β-Mn-phase shows enrichment of chromium additionally to the enrichment of aluminum and nickel. However, the formation of a third phase with increasing content of manganese can be locally observed within the β-Mn-phase. So far, this has not been shown for the FMAN alloy. As in-depth analysis is beyond the scope of the present work, this needs to be the subject of further studies, where thermodynamic calculations and transmission electron microscopy will have to be exploited to provide details on the nature of this phase.

The microstructure of the polycrystalline condition is displayed in Figure 4. The accelerated cooling rate results in a polycrystalline condition, where the matrix is characterized by an austenitic (bcc) phase structure. Along the grain boundaries, the formation of the
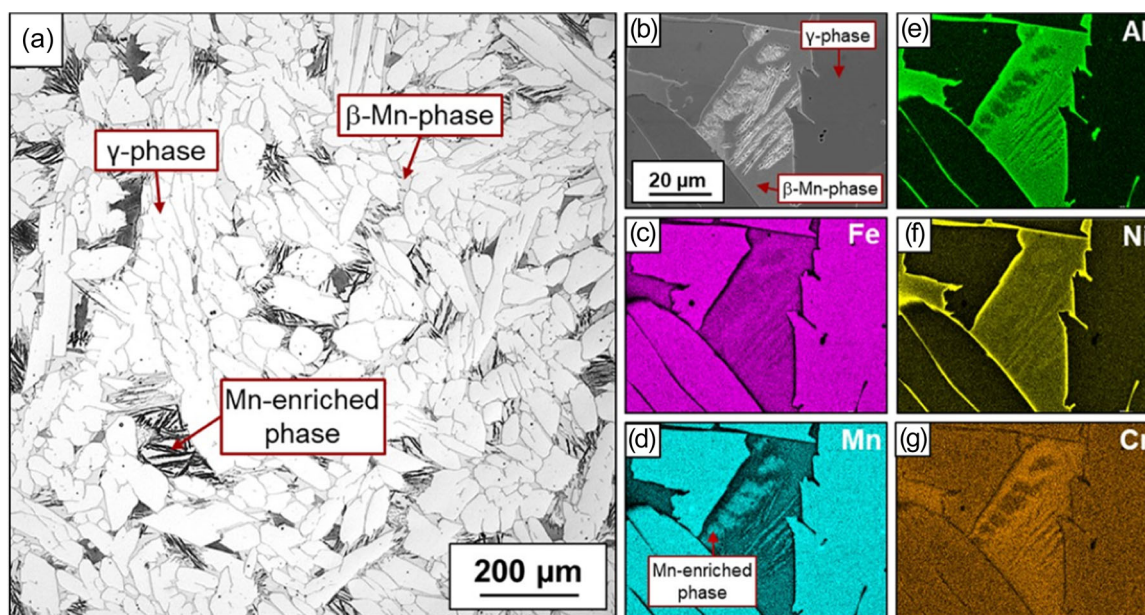

FIGURE 3 Microstructure of the Fe–Mn–Al–Ni–Cr furnace-cooled condition: (a) optical micrograph, (b) high-resolution SE image of the phase boundaries between the β-Mn-phase and the γ-phase, (c–g) corresponding EDS maps for iron (Fe), manganese (Mn), aluminum (Al), nickel (Ni), and chromium (Cr). [Color figure can be viewed at wileyonlinelibrary.com]

FIGURE 4 Microstructure of the Fe–Mn–Al–Ni–Cr polycrystalline condition: (a) optical micrograph, (b) high-resolution SE image depicting the γ-phase in the direct vicinity of a grain boundary, (c–g) corresponding EDS maps for iron (Fe), manganese (Mn), aluminum (Al), nickel (Ni), and chromium (Cr). [Color figure can be viewed at wileyonlinelibrary.com]
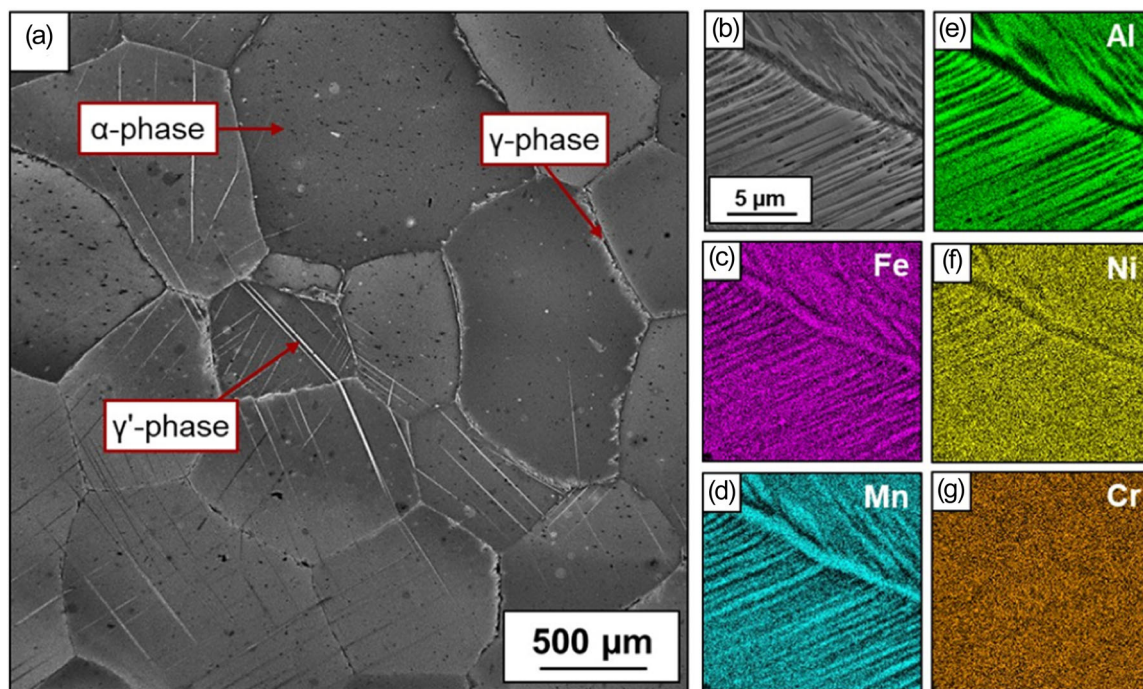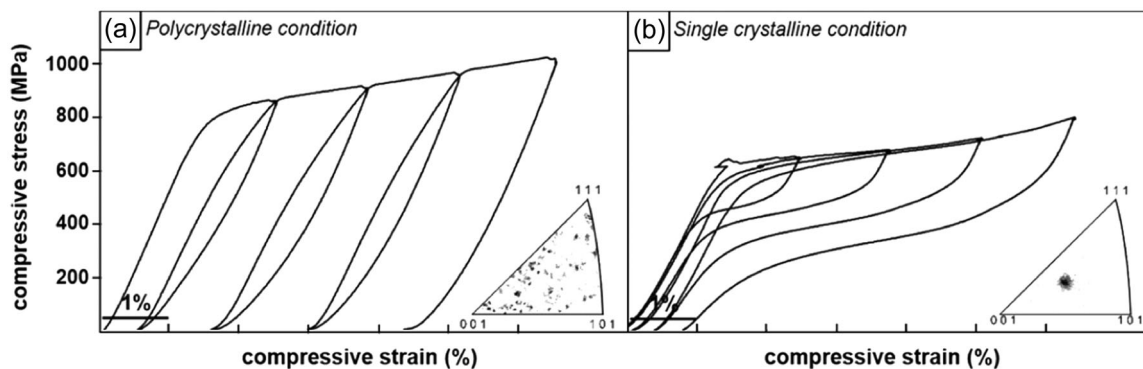

FIGURE 5 Superelastic response of Fe–Mn–Al–Ni–Cr compression specimens in (a) polycrystalline condition and (b) single crystalline condition. Insets in (a) and (b) display the corresponding inverse pole figure (IPF) maps detailing the overall distribution of grain orientations for every data point for each condition in load direction.

γ-phase can be observed and martensite plates are formed irregularly distributed within the grains. The EDS element maps (Figure 4c–g) reveal that the γ-phase, in line with the findings presented for the furnace-cooled condition, is characterized by a higher concentration of iron and manganese. Chromium appears to be distributed evenly. For the FMAN–Cr single crystalline condition, a similar microstructure as compared to the FMAN alloy[20] was observed, with an austenitic α matrix and a few γ′-martensite plates mainly formed near the surface of the specimens. As

no additional features were found, this condition is not depicted here for the sake of brevity.

To investigate the functional behavior of the FMAN–Cr alloy, incremental strain tests up to 6% compressive strain were conducted focusing on the polycrystalline and single crystalline conditions. The furnace-cooled condition is not relevant for any application and was therefore not tested. The resulting stress-strain curves are displayed in Figure 5. The grain orientations of the specimens with respect to the loading direction are highlighted in the inverse pole figures

shown as insets in Figure 5a,b. Similar to the solution annealed, polycrystalline FMAN tension specimens tested in the study by Vollmer et al.,[5] the polycrystalline condition displays poor superelastic behavior (Figure 5a). In contrast, the single crystalline condition shows good reversibility in the superelastic tests (Figure 5b), that is, a transformation stress of about 650 MPa and a recovery strain of 5.2% at a maximum applied strain of 6%. The FMAN alloy with similar crystallographic orientation is characterized by a similar mechanical behavior under compression, with a critical stress of about 480 MPa and 5.7% recoverable strain at a maximum applied strain of 8%.[11]

In order to investigate if the alloyed chromium content of 1.5 at% has a more significant impact on the corrosion behavior than on the functional properties, different electrochemical corrosion tests have been conducted. The three specific microstructural conditions introduced before were investigated. This allowed to directly compare the results elaborated here with those obtained in a previous study, where the focus was on the assessment of the corrosion properties of the FMAN alloy.[20] The polarization curves are presented in Figure 6. While the black lines represent the FMAN–Cr alloy, the light gray lines correspond to the polarization curves of the FMAN alloy, which were recompiled from the study by Frenck et al.[20] The potential values derived from these curves are listed in Table 1. The value E_{OCP} represents the potential at equilibrium determined after 24 h of immersion time immersion time. Here, a more negative potential indicates a higher susceptibility to corrosion.[32] All microstructural conditions of the FMAN–Cr alloy are characterized by a higher E_{OCP} compared to the corresponding FMAN conditions. This clearly indicates that the overall electrochemical activity of the alloy already decreases with the addition of 1.5 at% chromium. E_{corr} marks the transition between cathodic and anodic polarization. At this point, similar to E_{OCP}, both currents are in equilibrium.[33] A relatively high difference between E_{OCP} and E_{corr} can be observed for all tested conditions. This most likely results from the cathodic polarization during the potentiodynamic scan. The potential E_b indicates the breakdown potential, at which a passive system starts to corrode.[33] Although the values being representative of E_{corr} for the FMAN–Cr furnace-cooled condition is more positive than for the FMAN alloy, the curve progression is rather similar (Figure 6a). At the beginning of the anodic reaction, the curves are characterized by only a minor increase in current density, however, no distinct passive region can be observed. From about −400 mV (vs. SCE) the current density of the FMAN–Cr specimen increases exponentially, resulting in a pronounced anodic metal dissolution process. The polarization curves of the
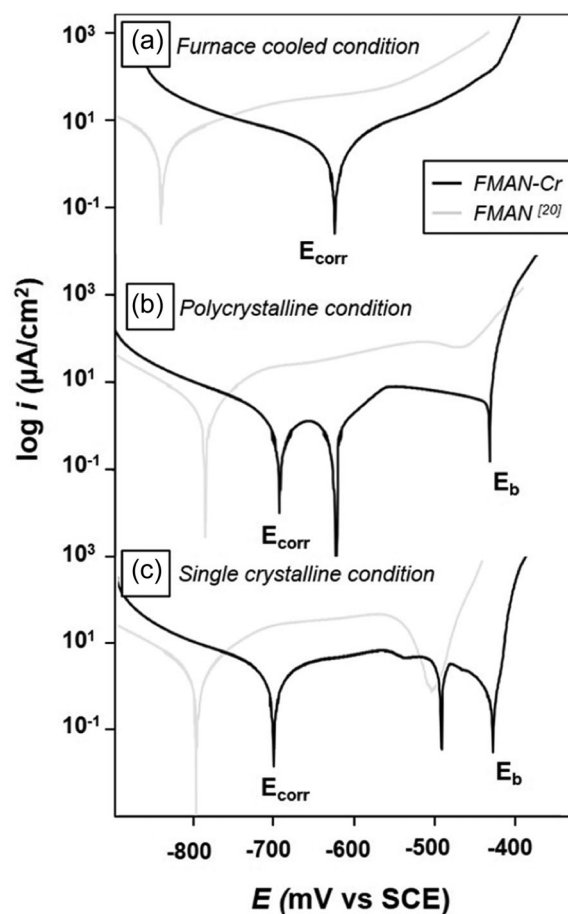

FIGURE 6 Electrochemical polarization curves of the (a) furnace-cooled conditions, (b) polycrystalline conditions, and (c) single crystalline conditions. E_{corr} marks the potential, at which the cathodic and anodic reactions are in equilibrium. E_b points at the breakdown potential. The gray curves, which display the polarization behavior of the FMAN alloy, have been recompiled from the study by Frenck et al.[20]

FMAN–Cr specimens shown in Figure 6b,c are characteristic of unstable passive behavior.[32] Secondary corrosion peaks as seen for the FMAN–Cr alloy at a potential of −620 mV (vs. SCE) and −490 mV (vs. SCE) for the polycrystalline condition (Figure 6b) and single crystalline condition (Figure 6c), respectively, result from a spontaneous cathodic reaction during the anodic polarization process.[32] A similar, though not as pronounced, reaction can be observed for the single crystalline FMAN condition[20] (also displayed in Figure 6c, gray line). For both FMAN–Cr conditions, the unstable passive region ranges from −700 mV (vs. SCE) to approximately −430 mV (vs. SCE). After reaching the breakdown potential E_b the corrosion rates increase rapidly due to severe corrosion attacks, those being fairly local in nature as will be shown later in the present paper.

TABLE 1 Electrochemical parameters extracted from the POL and OCP measurements.

	E_{OCP} (mV vs. SCE) after 24 h	E_{corr} (mV vs. SCE) after 24 h	i_{corr} (μA/cm^2)	E_b (mV vs. SCE) after 24 h
Furnace-cooled condition				
Fe–Mn–Al–Ni	−630.3[20]	−842.0[20]	2.614[20]	–
Fe–Mn–Al–Ni–Cr	−571.8 (±5)	−634.5 (±10)	2.010 (±0.8)	–
Polycrystalline condition				
Fe–Mn–Al–Ni	−648.3[20]	−788.0[20]	1.409[20]	–
Fe–Mn–Al–Ni–Cr	−597.3 (±15)	−728.7 (±30)	0.6942 (±0.08)	−436.0 (±5)
Single crystalline condition				
Fe–Mn–Al–Ni	−652.1[20]	−797.9[20]	1.442[20]	−502.2[20]
Fe–Mn–Al–Ni–Cr	−602.0 (±5)	−703.1 (±5)	1.433 (±0.2)	−431.0 (±5)

Note: E_b for the first three conditions listed was not determined, because the corresponding polarization curves do not indicate a clear breakdown potential. Current density within the passive range has not been analyzed as the secondary peak is characterized by a rapid decrease in current density, eventually hindering reliable evaluation.

FIGURE 7 Optical micrographs of the microstructures after polarization tests of (a) the furnace-cooled condition and (b) the polycrystalline condition. [Color figure can be viewed at wileyonlinelibrary.com]
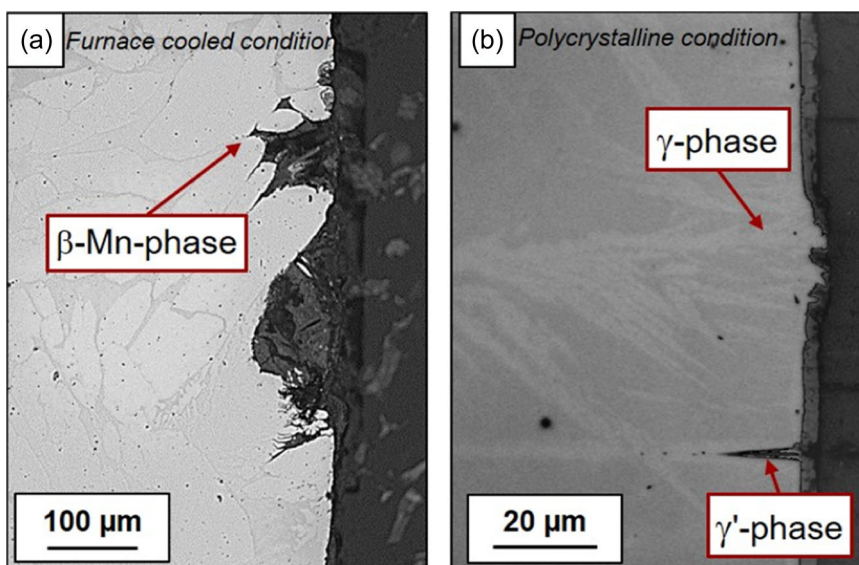

Figure 7 displays OMs of cross-sections of a furnace-cooled (Figure 7a) and a polycrystalline condition (Figure 7b) after the polarization tests. Both micrographs reveal obvious traces of corrosion damage. The furnace-cooled condition is characterized by a distinct selective corrosion attack of the β-Mn-phase. Such a selective corrosion attack in a multiphase system usually results from a potential difference between the existing phases.[34] As shown in Figure 3, the phases are distinguished by a difference in the chemical composition with enrichment of aluminum, nickel and chromium in the β-Mn-phase. It is well known that such local differences in chemical composition result in potential differences.[34] As the β-Mn-phase was preferentially dissolved, it is reasonable to assume that the γ-phase has

better corrosion resistance and, thus, acts as the cathodic part in a galvanic corrosion process. Eventually, this results in a higher corrosion rate of the β-Mn-phase. Similar corrosion phenomena have been reported in a previous work focusing on the FMAN alloy.[20] However, compared to the corrosion attack in the case of the FMAN alloy, where a penetration depth of the corrosion damage up to 400 μm was observed,[20] the deepest corrosion defect observed for the FMAN–Cr alloy is less than 100 μm. The EDS map in Figure 3g displays an enrichment of chromium in the β-Mn-phase. Presumably, this chemical difference (in relation to FMAN) reduces the potential difference between the γ-phase and the β-Mn-phase, which in return is associated with an improved corrosion behavior and lower penetration

depths of the corrosion damage. In addition, the furnace-cooled FMAN–Cr condition is characterized by a higher γ-phase fraction compared to the FMAN alloy. By reducing the amount of the β-Mn-phase, the quantity of local corrosion elements will also be reduce, which further results in a reduction of the corrosion rate. An additional influence of the third phase, that is, the Mn-enriched phase, could not be observed based on analysis of the OM images. Figure 7b shows the cross-section of a polycrystalline condition being characterized by various γ′-martensite plates distributed arbitrarily within the grains and an accumulation of γ-phase at the grain boundaries. The highlighted traces of corrosion damage clearly indicate uniform corrosion of the austenitic grain matrix (α-phase), with corrosion pits being located alongside the γ′-martensite plates. The EDS maps shown in Figure 4 reveal a similar chemical distribution as in the case of the furnace-cooled condition, that is, enrichment of iron and manganese in the γ-phase. The γ-phase again appears to be the more noble phase. As highlighted in Figure 7b the α-phase is preferentially attacked. However, due to the strict localization of the γ-phase at the grain boundaries, the corrosive attack is much more homogeneous at the surface compared to the furnace-cooled condition. The preferential corrosion attack of the martensitic plates most probably results from the high defect density being characteristic for martensite.[20,35] No difference in terms of the chemical composition could be observed between the austenitic α-phase and the γ′-martensite plates.

Corrosion pits alongside the γ′-martensite plates were also observed for the single crystalline condition. Figure 8 displays an SE image of the cross-section of a single crystalline condition after polarization. The insets show EDS maps related to the same image. The corrosion layer on the surface is characterized by two layers with different chemical compositions. The layer directly attached to the surface consists only of iron and manganese and is labeled as Layer 2. Layer 1 appears to be formed as a mixed-oxide layer consisting primarily of oxygen, nickel and aluminum, however, also partly contains chromium as well as iron and manganese. The results are similar to the findings reported for the single crystalline FMAN condition, where two different corrosion processes were observed. The first one was attributed to the dissolution of iron and manganese atoms in the corrosion pits along the martensite plates and the second one to the formation of a similar oxide layer consisting mainly of aluminum and nickel.[20,21]

To further investigate the reactions on the surface and the influence of chromium on the formation of the oxide layer EIS measurements have been conducted on a single crystalline condition for the FMAN–Cr alloy as
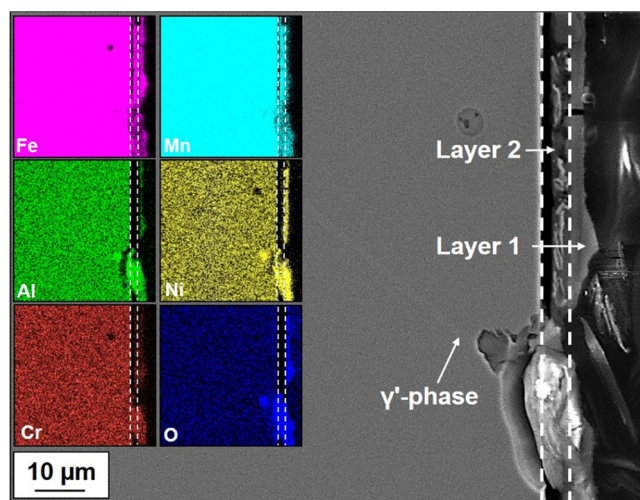

FIGURE 8 SEM image of the single crystalline condition after polarization tests, highlighting the corrosion damage due to micropitting. The insets display EDS maps for iron (Fe), manganese (Mn), aluminum (Al), nickel (Ni), chromium (Cr), and oxygen (O). [Color figure can be viewed at wileyonlinelibrary.com]

well as the FMAN alloy. Figure 9 shows the EIS results depicted as Bode plots. The plots were analyzed using the equivalent circuit model, shown as an inset in Figure 9a. The model is based on circuits that are often used in open literature for the simulation of corrosion processes for materials that are characterized by a passive oxide layer and locally occurring pitting corrosion.[36–39]

In the circuit model R_s represents the solution resistance, R_1 is the resistance of the oxide layer (Layer 1), and R_2 is the charge transfer resistance (Layer 2). Constant phase elements CPE_1 and CPE_2 represent the capacitance of the passive film and the charge transfer process caused by the corrosion pits, respectively. CPEs are usually used for considering a high surface roughness, porosity, or a non-uniform distribution of surface currents.[40,41] The CPE elements instead of an ideal capacitor were primarily chosen because of the actively contributing pitting processes, which were observed for both examined alloys alongside the martensite plates. The phase angle curve (Figure 9b) also indicates that a non-ideal passivating system is present since the largest observed phase angle in the Bode plot for the FMAN–Cr alloy was −72° at a frequency of about 50 Hz. According to the literature, a phase angle of −90° is characteristic for a capacitance response, which can be observed for ideal passivating systems.[32,40] The observed maximum phase angle is much lower than −90°, clearly indicating that inhomogeneity of the surface layer leads to the deviation of the electrode from ideal capacitance characteristics. However, the larger phase angle for the FMAN-Cr alloy (72°/50 Hz) compared to the FMAN
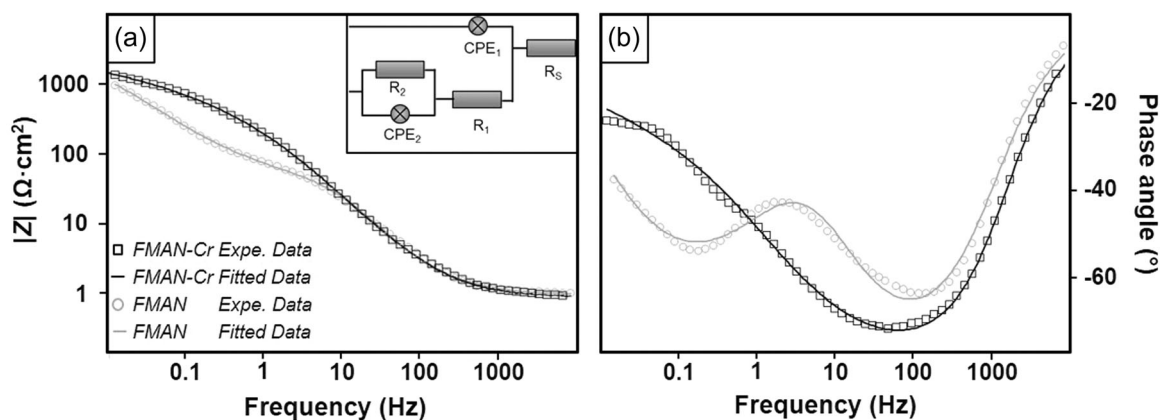
FIGURE 9 EIS measurements for single crystalline FMAN and FMAN–Cr after immersion in a 5.0 wt% NaCl solution for 24 h: (a) Bode plot-impedance spectra and (b) Bode plot-phase angle. The inset in (a) displays the proposed equivalent circuit model. See text for details.

TABLE 2 Electrochemical parameters extracted from the EIS measurements using the equivalent circuit model are shown as an inset in Figure 9a.

| | R_s ($\Omega \cdot cm^2$) | R_1 ($\Omega \cdot cm^2$) | CPE$_1$ | | R_2 ($\Omega \cdot cm^2$) | CPE$_2$ | |
			α_1	C_1 (S·s$^\alpha$ cm^2)		α_2	C_2 (S s$^{\alpha^*}$ cm^2)
Fe–Mn–Al–Ni	0.289	22.16	0.862	0.0015	858.87	0.700	0.00871
Fe–Mn–Al–Ni–Cr	0.265	50.00	0.880	0.0010	1216.93	0.385	0.00340

alloy (64°/160 Hz) indicates a more distinct capacitance characteristic of FMAN–Cr. It is thought that this occurs due to a more stable oxide layer on the surface resulting in increased resistance against penetration of aggressive ions. Furthermore, the sigmoidal impedance curve shape (Figure 9a) of the FMAN alloy can be related to a predominant charge transfer process.[32]

In general, the impedance of CPEs is defined as:

$$Z_{CPE}(\omega) = \frac{1}{(C \times (j \times \omega)^\alpha)} \quad (1)$$

where C is the CPE admittance value, ω is the angular frequency, and α is the phase angle index.[32,41] The CPE represents an ideal capacitance or a Warburg impedance, when $\alpha = 1$ or $\alpha = 0.5$, respectively. In line with the already discussed superior capacitance characteristic of the FMAN–Cr alloy, the α_1 component for the oxide layer (Layer 1) listed in Table 2 is characterized by a higher value than the α_1 component of the FMAN alloy. The second circuit (CPE$_2$/R_2), which is connected to R_1 in series, was added since both the FMAN and the FMAN–Cr systems have to account for two-time constants, caused by the dissolution of the oxide layer and the pitting corrosion process. With the addition of chromium to the FMAN alloy system the R_2 value increases (Table 2). This fact clearly demonstrates, in

accordance with the previous evaluations of the Bode plots, that the metal dissolution process at the metal–solution interface is reduced. The resistance of the oxide layer R_1 increases as well with the addition of chromium. This indicates that the passivation film impedance increases, eventually improving the protection against corrosion attack.[41]

4 | CONCLUSIONS

To improve the corrosion properties, while maintaining the functional properties of the Fe–Mn–Al–Ni (FMAN) SMA, a small amount of chromium (1.5 at%) has been added to the system (FMAN–Cr). Functional properties were investigated using incremental strain tests with a maximum strain of 6%. To assess the behavior in a corrosive environment, electrochemical corrosion tests (OCP, POL, EIS) in a neutral 5.0 wt% NaCl solution (pH 7) have been conducted using a conventional three-electrode cell. Since previous studies revealed that the corrosion behavior, as well as the functional properties of the FMAN alloy, are strongly dependent on the prevailing microstructure and, thus, on phases being present in the material, all experiments were performed on different microstructural conditions. From the findings elaborated in the present work the following conclusions can be drawn:

- In the incremental strain tests, good superelastic reversibility of the single crystalline condition could be observed, which is absolutely on the performance level of the well-established FMAN alloy.
- The corrosion tests revealed that even a small amount of chromium (1.5 at%) added to the FMAN alloy can improve the corrosion behavior and, eventually reduce corrosion damage to the material.
- All investigated microstructures are characterized by a selective corrosion attack. In the case of the single crystalline condition and the polycrystalline condition pitting corrosion along the γ'-martensite plates was observed.
- The latter mechanism might become an issue in the case of application, when a construction under loading is exposed to a corrosive environment. Thus, future studies will have to focus on stress corrosion in the FMAN system.

CONFLICT OF INTEREST
The authors declare no conflict of interest.

DATA AVAILABILITY STATEMENT
The data that support the findings of this study are available from the corresponding author upon reasonable request.

ORCID
Johanna-Maria Frenck https://orcid.org/0000-0003-2624-2916

REFERENCES
[1] T. Sawaguchi, T. Maruyama, H. Otsuka, A. Kushibe, Y. Inoue, K. Tsuzaki, *Mater. Trans.* **2016**, *57*, 283.
[2] A. Cladera, B. Weber, C. Leinenbach, C. Czaderski, M. Shahverdi, M. Motavalli, *Constr. Build. Mater.* **2014**, *63*, 281.
[3] M. Vollmer, A. Bauer, J.-M. Frenck, P. Krooß, A. Wetzel, B. Middendorf, E. Fehling, T. Niendorf, *Eng. Struct.* **2021**, *241*, 112430.
[4] T. Omori, K. Ando, M. Okano, X. Xu, Y. Tanaka, I. Ohnuma, R. Kainuma, K. Ishida, *Science* **2011**, *333*, 68.
[5] M. Vollmer, T. Arold, M. J. Kriegel, V. Klemm, S. Degener, J. Freudenberger, T. Niendorf, *Nat. Commun.* **2019**, *10*, 2337.
[6] T. Omori, M. Okano, R. Kainuma, *APL Mater.* **2013**, *1*, 032103.
[7] M. Vollmer, P. Krooß, M. J. Kriegel, V. Klemm, C. Somsen, H. Ozcan, I. Karaman, A. Weidner, D. Rafaja, H. Biermann, T. Niendorf, *Scr. Mater.* **2015**, *114*, 156.
[8] L. W. Tseng, J. Ma, S. J. Wang, I. Karaman, M. Kaya, Z. P. Luo, Y. I. Chumlyakov, *Acta Mater.* **2015**, *89*, 374.
[9] L. W. Tseng, J. Ma, M. Vollmer, P. Krooß, T. Niendorf, I. Karaman, *Scr. Mater.* **2016**, *125*, 68.
[10] T. Omori, H. Iwaizako, R. Kainuma, *Mater. Des.* **2016**, *101*, 263.
[11] L. W. Tseng, J. Ma, Y. I. Chumlyakov, I. Karaman, *Scr. Mater.* **2019**, *166*, 48.
[12] L. W. Tseng, J. Ma, S. J. Wang, I. Karaman, Y. I. Chumlyakov, *Scr. Mater.* **2016**, *116*, 147.
[13] M. Vollmer, M. J. Kriegel, P. Krooß, S. Martin, V. Klemm, A. Weidner, Y. Chumlyakov, H. Biermann, D. Rafaja, T. Niendorf, *Shape Mem. Superelasticity* **2017**, *3*, 335.
[14] A. Bauer, M. Vollmer, T. Niendorf, *Shape Mem. Superelasticity* **2021**, *7*, 373.
[15] P. La Roca, A. Baruj, C. E. Sobrero, J. A. Malarría, M. Sade, *J. Alloys Compd.* **2017**, *708*, 422.
[16] L. W. Tseng, J. Ma, B. C. Hornbuckle, I. Karaman, G. B. Thompson, Z. P. Luo, Y. I. Chumlyakov, *Acta Mater.* **2015**, *97*, 234.
[17] P. Huang, H. Peng, S. Wang, T. Zhou, Y. Wen, *Mater. Charact.* **2016**, *118*, 22.
[18] H. Ozcan, J. Ma, S. J. Wang, I. Karaman, Y. Chumlyakov, J. Brown, R. D. Noebe, *Scr. Mater.* **2017**, *134*, 66.
[19] M. Vollmer, C. Segel, P. Krooß, J. Günther, L. W. Tseng, I. Karaman, A. Weidner, H. Biermann, T. Niendorf, *Scr. Mater.* **2015**, *108*, 23.
[20] J.-M. Frenck, M. Vollmer, M. Mandel, L. Krüger, T. Niendorf, *Adv. Eng. Mater.* **2021**, *23*, 2000865.
[21] M. Mandel, V. Kietov, R. Hornig, M. Vollmer, J.-M. Frenck, C. Wüstefeld, D. Rafaja, T. Niendorf, L. Krüger, *Corros. Sci.* **2021**, *179*, 109172.
[22] A. M. de Sousa Malafaia, M. F. de Oliveira, *Corros. Sci.* **2017**, *119*, 112.
[23] T. Nishimura, *ISIJ Int.* **2014**, *54*, 1913.
[24] C. A. Della Rovere, J. H. Alano, R. Silva, P. Nascente, J. Otubo, S. E. Kuri, *Mater. Chem. Phys.* **2012**, *133*, 668.
[25] H. B. Peng, Y. H. Wen, B. B. Ye, N. Li, *Mater. Sci. Eng., A* **2009**, *504*, 36.
[26] B. C. Maji, C. M. Das, M. Krishnan, R. K. Ray, *Corros. Sci.* **2006**, *48*, 937.
[27] Y. Zhang, X. Zhu, S. Zhong, *Corros. Sci.* **2004**, *46*, 853.
[28] H. C. Lin, K. M. Lin, C. S. Lin, T. M. Ouyang, *Corros. Sci.* **2002**, *44*, 2013.
[29] X. Yuan, Y. Zhao, X. Li, L. Chen, *J. Mater. Sci. Technol.* **2017**, *33*, 1555.
[30] J. Xia, Y. Noguchi, X. Xu, T. Odaira, Y. Kimura, M. Nagasako, T. Omori, R. Kainuma, *Science* **2020**, *369*, 855.
[31] J. Tafel, *Z. Phys. Chem.* **1905**, *50U*, 641.
[32] R. G. Kelly, J. R. Scully, D. W. Shoesmith, R. G. Buchheit, *Electrochemical Techniques in Corrosion Science and Engineering*, Marcel Dekker Inc, New York **2003**.
[33] N. Sato, *Basics of Corrosion Chemistry*, Wiley, New York **2011**.

[34] E. Hornbogen, H. Warlimont, *Metallkunde: Aufbau und Eigenschaften von Metallen und Legierungen*, Springer, Berlin **2001**.

[35] H.-E. Bühler, W. Schwenk, *Werkst. Korros.* **1964**, *15*, 909.

[36] L. Feng, H. Yang, X. Cui, D.i Chen, G. Li, *RSC Adv.* **2018**, *8*, 6507.

[37] E. Volpi, A. Olietti, M. Stefanoni, S. P. Trasatti, *J. Electroanal. Chem.* **2015**, *736*, 38.

[38] R. G. Duarte, A. S. Castela, R. Neves, L. Freire, M. F. Montemor, *Electrochim. Acta* **2014**, *124*, 218.

[39] J. Pan, C. Leygraf, R. F. A. Jargelius-Pettersson, J. Linden, *Oxid. Met.* **1998**, *50*, 431.

[40] H. Herrera Hernández, A. M. Ruiz Reynoso, J. C. Trinidad González, C. O. González Morán, J. G. Miranda Hernández, A. Mandujano Ruiz, J. Morales Hernández, R. Orozco Cruz, in *Electrochemical Impedance Spectroscopy* (Eds: M. El-Azazy, M. Min, P. Annus), IntechOpen, London, UK **2020**.

[41] Q. Li, *Int. J. Electrochem. Sci.* **2020**, *167*, 11700.

SUPPORTING INFORMATION

Additional supporting information can be found online in the Supporting Information section at the end of this article.